Assembled Surface-Anisotropic Colloids as a Template for a Multistage Catalytic Membrane Reactor

Jung Hun (Kevin) Song and Ilona Kretzschmar*

Department of Chemical Engineering, The City College of New York, Steinman Hall, 140th Street & Convent Avenue, New York, New York 10031

ABSTRACT A polymeric catalytic membrane reactor (CMR) is fabricated using alternating assemblies of surface-anisotropic (sa-) and plain (p-) polystyrene (PS) colloids as a template. We report the preparation of TiO_2 sa-PS colloids by physical vapor deposition of titanium onto a colloidal monolayer in an oxygen-rich environment and employ the modified colloids as a means to deliver the TiO_2 catalyst to the CMR pores. sa-PS and p-PS colloids are assembled into alternating cylindrical sections inside a microcapillary followed by infiltration and curing of a liquid polymer precursor in the interstitial space of the assembly. Subsequent organic solvent treatment results in a cylindrical porous CMR with embedded TiO_2 caps. TiO_2 cap embedment, composition and surface morphology, surface pore structure, and cross-sectional integrity are analyzed using variable-pressure scanning electron microscopy, transmission electron microscopy, and X-ray photoelectron spectroscopy.

KEYWORDS: colloidal template • porous materials • fibers • polystyrene • multisectional • reactive separation • multistage • catalyst • titanium dioxide • titanium • physical vapor deposition • Janus particle

INTRODUCTION

Process intensification (PI) promises new modes of enhancement in reaction engineering by drastically improving the technique and operation of reactive separation (1). Novel and innovative technology provides a pathway for process improvement by reducing the equipment volume, processing time, energy consumption, and ultimately operational costs (2). A notable PI is a catalytic membrane reactor (CMR), where the unit operations of separation and reaction are combined into one spacial and temporal unit. CMRs offer numerous advantages in unit operations including (i) a chemical equilibrium shift brought on by the continuous removal of a product from a reaction mixture to enhance the yield, (ii) decreased product inhibition and increased overall reaction rate by the continuous removal of a product, (iii) reduced side reactions through lower operating temperatures, and (iv) facilitated separation of the reactants and products through membrane separation (3, 4).

Polymeric CMRs, unlike metallic or inorganic CMRs, are being widely explored for various processes because of their economic efficiency and tailorable properties (3, 5). Despite their advantageous process enhancement, polymeric CMRs are limited by the operating conditions; i.e., most often they are inoperable at an operating temperature above 250 °C. However, even with this limitation, polymeric CMRs have numerous applications in volatile organic compound degradation, hydrogenation, and other low-temperature catalytic reactive operations (6).

The application, performance, and efficiency of a polymeric CMR depend on the distribution of the selected catalyst and the porous structure of the CMR (7). These properties may be addressed and tailored by employing polymeric colloids in the fabrication of a CMR. For example, three-dimensional colloidal assemblies have been widely applied to template and synthesize ordered porous materials (8). On the other hand, surface-anisotropic modification of colloids has gained immense interest because of the wide range of modifications available (9, 10). Combining colloidal templating and surface-anisotropic modification techniques yields a *surface-anisotropic colloidal delivery and template system* (sa-CDTS) for CMR synthesis, where the catalyst material distribution and porous structure are precisely controlled.

One of the many functional catalyst materials available that may be utilized in a CMR is titanium (Ti) and its oxides (Ti_xO_y) (3, 11). Among multiple oxidation states of Ti_xO_y ($x = 1, 2$; $y = 1-3$), TiO_2 is the principle component of all oxides (12). TiO_2 has been reported to form on the surface of bulk Ti within milliseconds of exposure to air (13). With prolonged exposure to oxygen and increased transport of Ti from the suboxide layer to the surface, a natural 10 nm thin TiO_2 layer is formed (12−15). In addition to the naturally forming TiO_2, many processes including thermal plasma (16), electrochemical (14), and sputter deposition (17) as well as electric-arc physical vapor deposition (PVD) (18) have been developed to induce the formation and deposition of TiO_2 films. Further, TiO_2 is extensively researched for its high photocatalytic activity at low temperature and economic

* Corresponding author. E-mail: kretzschmar@ccny.cuny.edu.
Received for review April 28, 2009 and accepted June 24, 2009

DOI: 10.1021/am900286k

efficiency in comparison to rare metal and other metal oxide catalysts (12, 19, 20). The research previously published focused on utilization of the anatase phase of TiO_2 because it is the more catalytically active phase (20). However, recently other phases have been explored including rutile, brookite, and amorphous, as well as the combination of different phases, and the doping of TiO_2 with different elements to form heterogeneous TiO_2 catalysts with tailored photocatalytic properties (21−24).

In this article, we report a CDTS-based methodology for the fabrication of ordered, porous CMRs using the convective assembly of surface-anisotropic colloids modified with a PVD-deposited TiO_2 catalyst. We show CMRs fabricated with repeating segments of plain and catalyst-loaded porous regions. Microcapillaries are used as templates for the colloidal assemblies, resulting in a cylindrical CMR. To enable both the characterization and the study of the CMR structure, the microcapillaries and colloids are removed in succession prior to the analysis, yielding porous fibers. Surface modification, catalyst embedment and orientation, and surface and cross-sectional pore structure are characterized by variable-pressure scanning electron microscopy (vp-SEM). Energy-dispersive X-ray spectroscopy (EDS) available on vp-SEM and X-ray photoelectron spectroscopy (XPS) are used for characterization of the catalyst composition.

EXPERIMENTAL SECTION

Materials. Sulfate-terminated polystyrene (PS) colloids with 2.5 ± 0.1 μm diameter and 8% (w/v) concentration in aqueous form were purchased from Invitrogen. A poly(methyl methacrylate) (PMMA) capillary of 50 ± 2.5 μm inner diameter (i.d.) on spools of 1 m was purchased from Paradigm Optics. Titanium sponges with diameters ranging from 2 to 12 mm were purchased from Aldrich. Ultraviolet (UV)-light-curable polyurethane liquid prepolymer NOA 60 was purchased from Norland Optics. Deionized (DI) water was obtained from a Millipore Milli-Q unit. Concentrated sulfuric acid and NOCHROMIX were purchased from Acros Chemical and Godax Laboratories, respectively. Mechanical grade silicon wafers were purchased from University Wafers. Anhydrous stabilized tetrahydrofuran (THF) and certified ACS-grade toluene were purchased and used as received from Acros Chemical and Fisher Scientific, respectively. A custom blend of a 3:1 Ar/O_2 mixture was synthesized by and purchased from Airgas Inc.

Preparation of the Anisotropic Colloidal Delivery System. A total of 100 μL of a PS colloidal solution is washed three times with 1000 μL of DI water by ultrasonication followed by centrifugation. The supernatant water is extracted to remove surfactants and to obtain a 16% (w/v) concentrated colloidal solution. A total of 10 μL of the concentrated colloidal solution is placed between two acid-cleaned microscopic glass slides mounted at an angle on a motorized stage PHD 2000 (Harvard Apparatus). The trapped colloidal solution is dragged (a modified Prevo and Velev process) (25) at a speed of 6 mm/min by the motion of the top glass slide. Monolayers with subpacked to close-packed colloids are obtained and subsequently used for the deposition of TiO_2 by PVD (11). Approximately, 0.02 ± 0.01 g of titanium sponge is placed in the three-strand tungsten wire basket (Ted Pella No. 76) inside of the PVD unit (Cressington 308). With monolayer samples placed on a stage underneath the basket (the sample-to-source distance is approximately 15 cm), the PVD chamber is pumped until a pressure of 5×10^{-4} Pa is reached. A 3:1 Ar/O_2 gas mixture is used to purge the evaporator chamber and then consistently leaked into the chamber to reach an evaporation pressure of 0.5 Pa. An average TiO_2 deposition rate of 0.3 nm/s is used to obtain a nominal thickness of 30 ± 3 nm. In addition to the monolayer deposition, TiO_2 films are deposited under equivalent conditions on both 1 and 9 cm^2, acid-cleaned silicon wafers for X-ray spectroscopic and diffraction analysis (see below).

Surface Enhancement. The TiO_2-capped colloids on the glass slides are submerged under 200 mL of DI water and ultrasonicated (40 kHz) for 15 min to lift off the colloids. A dilute suspension with a concentration of less than 0.01% (w/v) is obtained. The suspension is concentrated to 20 mL of 0.1% (w/v) by repeated centrifugation and supernatant removal. For external surface enhancement of the TiO_2 cap, 0.21 g of 4-aminobutanoic acid (ABA) is added to the 0.1% (w/v) colloidal suspension, resulting in a 100 mM concentration. The ABA colloidal suspension is allowed to interact with the TiO_2 surface for approximately 24 h. The ABA colloidal suspension is then centrifuged to remove the supernatant, which contains the excess ABA. DI water is added to the sediment, and the ABA-modified colloids are resuspended. The final ABA-modified colloidal suspension of 1% (w/v) is prepared for colloidal assembly by an identical process of centrifugation and removal of the supernatant.

Fabrication of TiO_2-Loaded CMRs. When the protocol developed by Song et al. is applied (8), cylindrical colloidal assemblies with alternating sections of plain and TiO_2-capped colloids are convectively assembled in a microcapillary. In brief, a droplet of an aqueous colloidal suspension is placed at one end of a microcapillary and allowed to fill the microcapillary. Solvent evaporation at the opposite end creates a convective flow of particles into the microcapillary, leading to the formation of a colloidal crystal inside the capillary upon drying. Subsequently, the interstitial spaces formed within the multisectional assemblies are infiltrated with the UV-curable prepolymer NOA 60 for approximately 48 h. Prepolymer-infiltrated multisectional assemblies are cured under 365 nm UV light for 2 h at 730 μW/cm^2 (Spectroline A14 VS) and an additional 30 min at 8000 μW/cm^2 (Dreve Polylux500). The cured matrix is subsequently treated with repeated 5 min dips in THF and washes with toluene. The PMMA capillary and colloids are removed during the solvent dissolution process, leaving the TiO_2 caps behind in the pores of the hardened, cylindrical CMR.

Imaging and Spectroscopy. SEM and high-resolution SEM (HR-SEM) images are obtained with Carl Zeiss EVO 40 and Supra 55 scanning electron microscopes, respectively. Both scanning electron microscopes are equipped with variable-pressure (vp) mode and EDAX EDS units. The vp mode available on the EVO 40 and Supra 55 scanning electron microscopes allows imaging of nonconductive samples without coating the samples with a conducting surface layer (Au or C) by admitting air or nitrogen into the vacuum chamber at a chamber pressure ranging from 35 to 40 Pa. The accelerating voltage used ranges from 10 to 13 kV and from 15 to 20 kV for EVO 40 and Supra 55, respectively.

For XPS, a 30 ± 3 nm thin film of TiO_2 is deposited onto a silicon wafer under the same conditions as those used for deposition on the colloidal monolayer. The XPS spectra of the thin coatings are recorded with a PHI 5500 spectrometer equipped with a hemispherical electron energy analyzer, a multichannel detector, and an Al Kα monochromator X-ray source running at 15 kV and 23.3 mA. The binding energy (BE) is internally referenced to the adventitious C 1s peak at 284.6 eV (26). High-resolution spectra are acquired with a pass energy of 23.5 eV and a BE resolution of 0.05 eV.

RESULTS

TiO_2 Surface-Anisotropic Colloids and TiO_2 Caps. PVD on a colloidal monolayer results in the partial

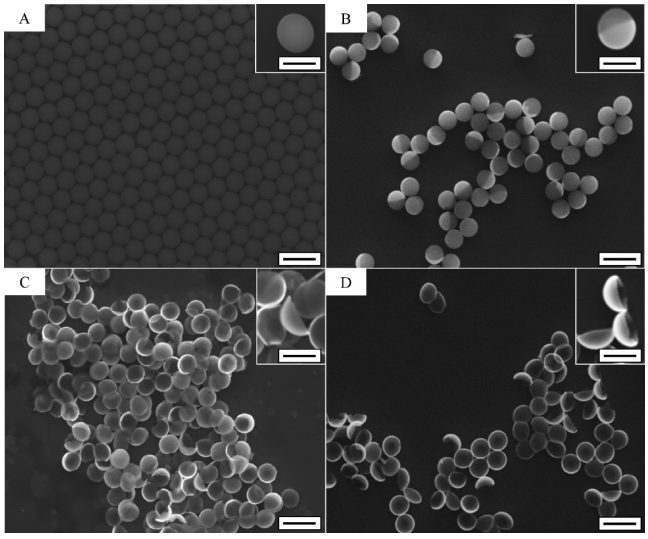

FIGURE 1. vp-SEM images of colloids and TiO_2 caps. (A) 2.5 μm p-PS colloids assembled into a close-packed monolayer. Inset: Higher magnification single p-PS colloid image. (B) TiO_2 sa-PS colloids. Inset: Image of a single TiO_2 sa-PS colloid showing a bright coating. (C) TiO_2 caps collected after solvent treatment. Inset: Higher magnification image of an aggregate of caps. (D) TiO_2 caps obtained after 550 °C calcination. Inset: Higher magnification image of three caps. The scale bars in all images and insets are 4 and 2 μm, respectively.

modification of the PS surface, and removal of the PS core results in stable TiO_2 caps (Figure 1). Figure 1A and its inset show images of a close-packed monolayer of plain PS (p-PS) colloids with 2.5 ± 0.1 μm diameter and an isolated p-PS colloid, respectively. Both images show spheres with a uniform surface contrast. The images in Figure 1B and its inset show surface-anisotropic PS (sa-PS) colloids drop-casted onto a silicon wafer and an isolated sa-PS colloid, respectively. Spheres with bright hemispherical- or half-moon-shaped areas on the colloid surface are discernible in both images. The brighter region is the TiO_2-deposited region on the colloids, whereas the darker region is the unmodified PS surface of the colloids. Figure 1C and its inset show an aggregate of TiO_2 caps collected after solvent treatment using THF. Randomly oriented TiO_2 caps with no obvious damage due to the solvent treatment are observed in both images. Figure 1D and its inset depict hemispherical TiO_2 caps obtained after calcination of drop-casted sa-PS colloids at 550 °C in air as the reference for fully oxidized TiO_2 caps (27). Some of the caps in Figure 1B–D show some unevenness in the rim due to the onset of shadowing inherent to the close packing of the colloids during TiO_2 deposition (28).

The surface compositions of p- and sa-PS colloids, solvent-treated and calcinated TiO_2 caps, and TiO_2 thin films are measured using EDS. Table 1 lists the weight percent compositions measured for the five different types of specimens and the EDS data for a cleaned silicon wafer as the reference. The values shown are the average of five measurements per specimen. The last column shows the ratio of titanium to oxygen signals. A comparison of the Ti/O data for sa-PS colloids, solvent-treated and calcinated TiO_2 caps, and TiO_2 thin films reveals that all four Ti/O ratios are ~1:2.2 and agree within 2%. The variation of the absolute values for titanium (Ti at 4.5 eV) and oxygen (O at 0.5 eV) from

Table 1. EDS Compositional Data of a Clean Wafer, p- and sa-PS Colloids, Solvent-Treated and Calcinated TiO_2 Caps, and TiO_2 Thin Films[a]

sample	C (%)	Si (%)	Ti (%)	O (%)	ratio (Ti/O)
clean wafer (reference)	<0.24	100.00	<0.10	<0.06	N/A
p-PS colloids	97.26	2.74	<0.10	<0.06	N/A
sa-PS colloids	93.36	0.50	1.90	4.24	1:2.23
solvent-treated caps	<0.24	89.48	3.21	7.31	1:2.28
calcinated caps	<0.24	58.50	12.82	28.68	1:2.24
film	<0.24	89.20	3.40	7.40	1:2.18

[a] All EDS measurements are based on a total weight percentage of 100 wt %.

Table 2. XPS BE (eV) Data for Ti $2p_{3/2}$, O 1s, and C 1s Taken from the NIST Database 26 Calibrated with Respect to Adventitious Carbon (adv C 1s = 284.8 eV)

sample	Ti $2p_{3/2}$ (eV)	O 1s (eV)	C 1s (eV)
TiC[a]	454.9	N/A	281.7
TiO[b]	454.6	N/A	N/A
Ti_2O_3[c]	457.8	529.6	N/A
TiO_2[b]	458.9	530.2	N/A
TiO_2 film[d]	458.9 ± 0.3	530.5 ± 0.5	N/A

[a] Galuska et al. (26, 42). [b] Gonbeau et al. (26, 43). [c] Werfel et al. (26, 44). [d] This work.

specimen to specimen is largely due to the different titanium oxide thicknesses of each type of specimen measured. All EDS analyses are performed on a cleaned silicon wafer, which does not show any traceable carbon, titanium, or oxygen peaks.

High-resolution XPS (HR-XPS) analysis is performed on five TiO_2 thin films ($d = 30 \pm 3$ nm) on silicon wafers. Table 2 shows reference values taken from the National Institute of Standards and Technology (NIST) database (26) for the Ti $2p_{3/2}$, O 1s, and C 1s XPS peak positions of titanium carbide (TiC) and various titanium oxides (TiO, Ti_2O_3, and TiO_2), as well as values measured for the freshly prepared TiO_2 thin films. All XPS values are calibrated with respect to adventitious carbon (C 1s) at a BE of 284.8 eV. The averages obtained for the freshly prepared thin film samples are 458.9 ± 0.3 eV for Ti $2p_{3/2}$ and 530.5 ± 0.5 eV for O 1s. These Ti $2p_{3/2}$ and O 1s BEs are in good agreement with the values listed for TiO_2 and clearly differ from the values expected for partially oxidized forms of titanium (e.g., TiO and Ti_2O_3), confirming the effective formation of TiO_2 when titanium is vapor-deposited in a 3:1 Ar/O_2 mixture. In addition, no XPS signal is detected in the range where the Ti $2p_{3/2}$ peak position for TiC is expected, indicating that the vapor deposition and solvent treatment do not lead to TiC formation on the TiO_2 catalyst.

Fabrication of the CMR via a TiO_2 Surface-Anisotropic Colloidal Delivery System. The actual shape of the CMR is determined by the geometric confinement defined by the initial template used for the colloidal assembly. A cylindrical geometry is chosen as the CMR template (Figure 2). Figure 2A shows an optical microscope image of a multisectional colloidal assembly in a 50 ± 2.5

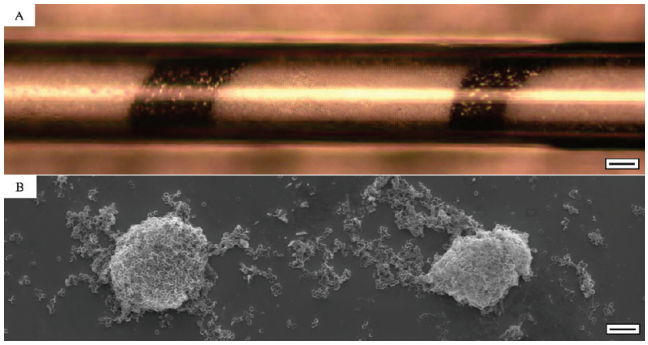

FIGURE 2. (A) Optical microscope image of a dried multisectional colloidal assembly fabricated using p-PS and TiO_2 sa-PS colloids. The dark segments with varying contrast depict regions of assembled TiO_2 sa-PS colloids. Scale bar = 15 μm. (B) SEM image of the multisectional assembly depicted in part A after calcination at 550 °C. Two piles of calcinated caps at 130 μm distance are observed. Scale bar = 15 μm.

μm (i.d.) PMMA capillary. The image depicts a colloidal assembly region with five alternating sections of p-PS and sa-PS colloids of the same size. Starting from left to right, alternating sections of 77 (p), 48 (sa), 140 (p), 31 (sa), and 77 (p) μm lengths are successively assembled inside the capillary. The five sections are distinguished by their color. The sa sections are dark and show a varying contrast along the length of the section, indicating a random orientation of the caps, whereas the p sections exhibit a uniform white color throughout the sections. Figure 2B shows an SEM image (same scale) of the assembly shown in Figure 2A after calcination at 550 °C. During calcination, the PS colloidal templates and PMMA capillary decompose into H_2O and CO_2, while the TiO_2 caps are left behind. Two distinguishable piles of TiO_2 caps and a distribution of caps between the piles are observed. The distance between the piles (130 μm) is comparable to the distance in the original assembly (140 μm). The distribution of caps between and around the piles is likely to result from instability of the cap assembly during the escaping of gas formed as part of the decomposition process.

CMRs with Bare TiO_2 Caps. After infiltration, curing, and solvent treatment of a colloidal assembly as shown in Figure 2A (8), CMRs fabricated using sa-PS and p-PS colloids show voids on the surface of the CMR section templated using the sa-PS colloids, while sections templated with p-PS particles are well formed. Figure 3A shows a section of a multisection CMR templated with sa-PS colloids. Several regions of incomplete polymer filling, i.e., voids, are observed on the CMR surface, while the cylindrical shape and diameter of the CMR remains consistent with the i.d. of the microcapillary template. Figure 3B depicts a high-magnification image of a void region, where the random orientation of the TiO_2 caps resulting from the CDTS is visible. No damage of the TiO_2 caps inside the CMR as a result of polymer infiltration, curing, and template removal is observed.

CMRs with Surface-Enhanced TiO_2 Caps. Increased wettability of the prepolymer and the sa-PS colloids ensures complete infiltration of the colloidal template. In Figure 4, a fully infiltrated, cylindrical polymeric CMR is

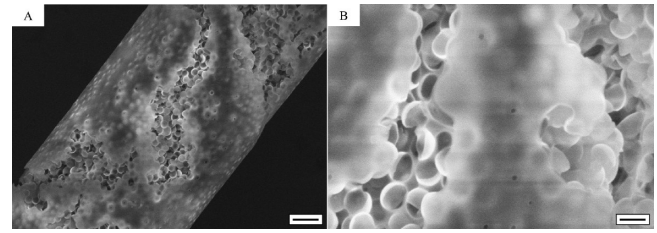

FIGURE 3. SEM images of the sa-PS-templated CMR region with voids after infiltration, curing, and solvent treatment. (A) Region of CMR with multiple voids resulting from incomplete infiltration of liquid prepolymer. Scale bar = 8 μm. (B) Higher magnification image of a void region showing intact TiO_2 caps inside the CMR. Scale bar = 2 μm.

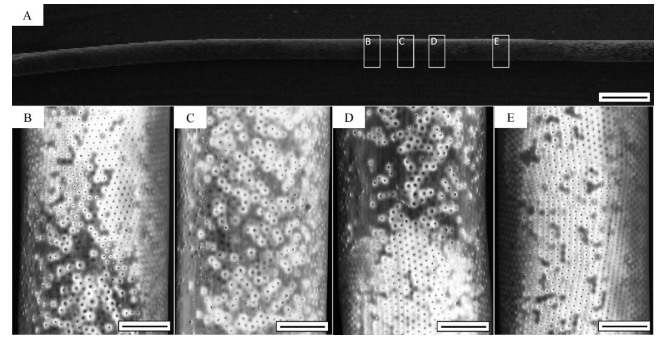

FIGURE 4. SEM images of a fully infiltrated CMR with three sections. (A) Large-scale view of CMR. Scale bar = 100 μm. (B) CMR region templated by p-PS colloids (top) and surface-enhanced sa-PS colloids (bottom). Scale bar = 14 μm. (C) CMR region templated with surface-enhanced sa-PS colloids. Scale bar = 14 μm. (D) CMR region templated by surface-enhanced sa-PS colloids (top) and p-PS colloids (bottom). Scale bar = 14 μm. (E) CMR region templated with p-PS colloids. Scale bar = 14 μm.

depicted that has been synthesized utilizing ABA surface-enhanced TiO_2 CDTS. Figure 4A depicts a large area view of a 1.8 mm section of a 1.5-cm-long polymeric CMR fiber with catalytic sections synthesized using plain and surface-enhanced TiO_2 CDTS. High-magnification images of several regions of the CMR are depicted in Figure 4B–E. Figure 4B shows the CMR's first interface synthesized using p-PS (top half) and surface-enhanced sa-PS colloids (bottom half). Surface pores in the region templated by p-PS colloids exhibit uniform pores indicating a close-packed arrangement of the colloids, whereas the section of the CMR templated using surface-enhanced sa-PS colloids shows an irregular pore arrangement and variation of the surface pores sizes but no void formation as observed for unmodified sa-PS colloids (Figure 3). Figure 4C shows a CMR region templated by surface-enhanced sa-PS colloids. An irregular arrangement of surface pores and a distribution of pore sizes comparable to that in the bottom half of Figure 4B are observed throughout the section, but again no voids are formed. In Figure 4D, the second interface between sections templated with surface-enhanced sa-PS (top half) and p-PS colloids (bottom half) is shown. Figure 4E shows a region with a well-ordered arrangement of pores and evenly distributed pores resulting from a close-packed p-PS colloidal template. The length of each section shown is approximately 77 μm.

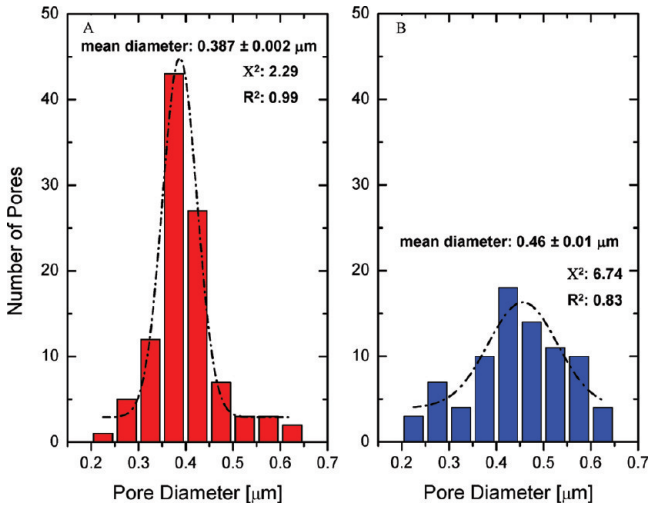

FIGURE 5. Surface pore diameter size distribution of CMR regions. (A) Surface pore diameter distribution of CMR regions templated by p-PS colloids. The dash-dotted line indicates a Gaussian fit of the distribution with $\mathbf{X}^2 = 2.29$ and $R^2 = 0.99$. (B) Surface pore diameter distribution of CMR regions templated by surface-enhanced sa-PS colloids. The dash-dotted line indicates a Gaussian fit of the distribution with $\mathbf{X}^2 = 6.74$ and $R^2 = 0.83$.

Surface Pore-Size Analysis. Figure 5 shows the surface pore diameter distribution obtained from five CMRs that have been fabricated using p-PS and surface-enhanced sa-PS colloids. Because of the curvature of the CMR, only the surface pores along the center (±10 μm) of the CMR are measured in each SEM image using *ImageJ* software. Each section measured is approximately 500 μm long. Figure 5 shows the distribution of surface pore diameters measured for the CMRs templated by p-PS colloids (Figure 5A) and surface-enhanced sa-PS colloids (Figure 5B). The surface pore diameters vary between 0.2 and 0.65 μm. Both distributions are fit with a Gaussian function (dash-dotted line). For the p-PS-templated section, the distribution is narrow and Gaussian-like ($\mathbf{X}^2 = 2.29$ and $R^2 = 0.99$) with an average pore size of 0.387 ± 0.002 μm, while the distribution of surface pore diameters in the section templated by surface-enhanced sa-PS colloids is much broader and not well fit by a Gaussian function ($\mathbf{X}^2 = 6.74$ and $R^2 = 0.83$) with an average pore size of 0.46 ± 0.1 μm.

EDS Characterization of Fibers. EDS measurements give insight into the width of the interfaces between p-PS- and sa-PS-templated sections by measuring the amount of titanium and oxygen in each section. Figure 6 shows a graph of the weight percent composition of titanium along the length of a multisectional CMR with alternating segments, as shown in Figure 4. The percent composition is based on the Ti−K-band data obtained with EDS. The fiber composition is analyzed every 20 μm starting approximately 40 μm prior to the interface depicted in Figure 4B. The effective electron-beam spot is estimated to be ≤3 μm in diameter. This estimate is obtained by measuring the size of a burned area on a sample resulting from prolonged exposure of the sample to the electron beam and EDAX electron flight simulation. The changes in the weight percentage observed between the 20−60, 120−160, 160−200, and 280−320 μm points show a gradual increase and decrease in the titanium

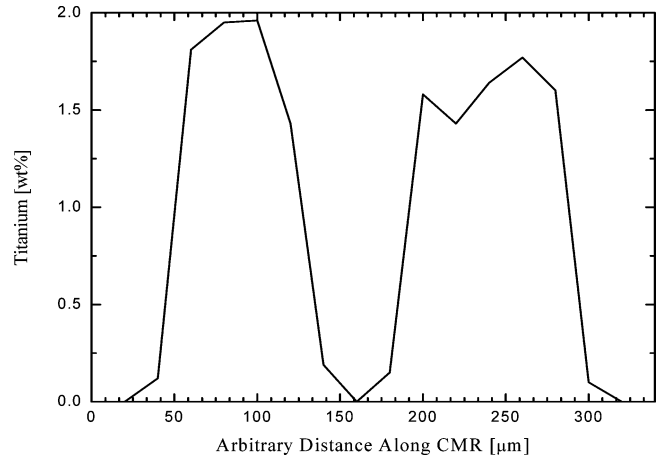

FIGURE 6. EDS weight percent composition measurement of titanium along the long axis of a CMR with two isolated TiO_2-templated sections.

weight percentage, indicating that the interfaces have widths of less than 40 μm, in good agreement with the interface width (28 μm) observed previously (8). The maximum percent compositions of titanium for the two titanium regions are 1.86 and 1.75 wt %.

DISCUSSION

The CDTS methodology enables control of various characteristics and properties of a CMR that affect the reactive separation process such as the reactor shape and size, pore structure, pore-size distribution, and catalyst distribution within the CMR (3, 4). In the following, we will discus the overall assembly and structure of the CMR, the catalyst cap distribution and orientation in the CMR, and the catalyst cap composition and structure.

The shape and size of the CMR are determined by the chosen application and the experimental setup it is used in. Once the outer geometric dimensions of the CMR are determined, obtaining a desired pore structure over a defined length is the next crucial characteristic that needs to be controlled for an effective CMR (3). A complete fiber with surface pores and defined TiO_2-loaded sections fabricated using CDTS is shown in Figure 4. The complete formation of a fiber is achieved through surface enhancement of the TiO_2 caps by reaction with the carboxyl group (−COOH) of ABA prior to assembly (29). The reactive adsorption of the carboxyl group on the TiO_2 cap allows the amine group of the ABA, located at the opposite end of the chain, to repel the colloids from each other in the suspension and facilitate the transport of the amine-based polyurethane prepolymer into the colloidal template during infiltration. As a result, the colloidal template is completely infiltrated compared to the CMR fabricated by employing unmodified sa-PS colloids (Figure 3).

Interestingly, the voids found on the CMR surface in Figure 3 offer some insight into the internal structure of the CMR and the stability of the TiO_2 caps. After repeated exposure to organic solvents, ultrasonication, and heat treatments during the CMR fabrication process, the caps turn out to be chemically, physically, and thermodynamically

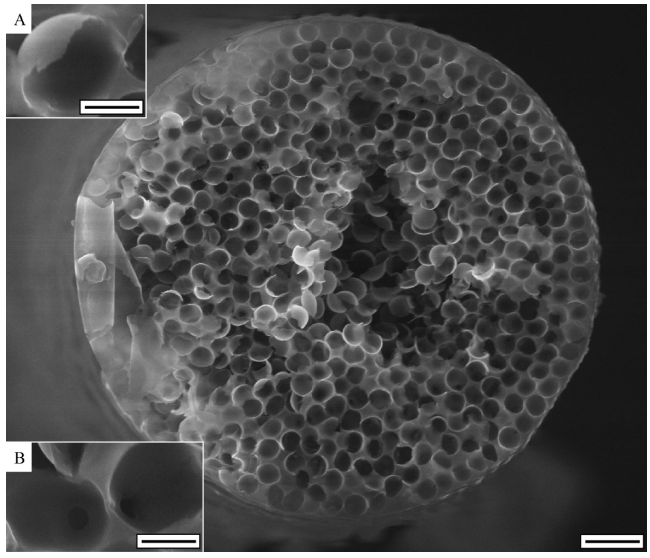

FIGURE 7. Cross-sectional view of a CMR section with TiO_2 caps. Scale bar = 5 μm. Insets A and B show higher magnification images of an embedded cap and interconnecting pores, respectively. Scale bar = 1 μm.

stable, as confirmed by the higher resolution SEM image in Figure 3B. The caps show no deformation or change in shape, which is in good agreement with previously reported findings (30).

The cap stability and inner pore structure is further confirmed by cross-sectional analysis of the CMR. Figure 7 shows a cross-sectional SEM image of a CMR sheared under liquid nitrogen along the section with the TiO_2 caps. Caps (inset A) and pores (inset B) are visible in the cross-sectional image, indicating that the TiO_2 caps are stable and the colloidal template has been completely infiltrated, leading to a porous structure throughout the fiber. In addition, the cross-sectional image reveals the random orientation of the caps within the CMR pores in good agreement with the random arrangement found before and after calcination of the multisectional colloidal template (Figure 2). Upon closer inspection, the structure of the interconnecting pores in the TiO_2 section seems to be less regular than that observed for plain colloids (8), in good agreement with the presence and orientation of caps in the pores (Figure 7, inset B). For example, if the caps of two colloids are in physical contact with each other or when a cap and an unmodified particle surface are in contact, no pore formation is expected, whereas when two unmodified particle surfaces are in contact, formation of a pore is expected (31, 32). Further, the CMR sections fabricated using TiO_2 CDTS show a random surface pore arrangement (Figure 4C), while the p-PS-colloid-templated sections show ordered surface pore structures (Figure 4E).

The quality and composition of the cap surfaces are crucial in obtaining a catalytically active surface. TiO_2 is deposited onto the PS colloids and later exposed to solvents to remove the colloidal template. During the process, diffusion and adhesion of carbon and/or other organic compounds may occur. Therefore, the compositional and structural analysis of the caps is required. EDS analysis (Table 1) indicates that caps resulting from solvent treatment contain no traceable carbon residue from either the solvents or the PS colloid. Further, the low temperature of the substrate at which the deposition is performed prevents the formation of TiC structures and diffusion of carbon into the deposited TiO_2, which occurs above 200 °C (33, 34). Note that the glass transition temperature of bulk PS is $T_g = 100$ °C (35). Lastly, no thermodynamic changes are expected during the short deposition time (~1.5 min) owing to the low thermal conductivity of TiO_2 ($k_{300\ K} < 1$ W m^{-1} K^{-1}) (36). A comparison of the EDS data for solvent-treated caps and the 30 nm TiO_2 thin films (Table 1) suggests that films and caps prepared under identical conditions have very similar compositions, as indicated by their comparable Ti/O ratios.

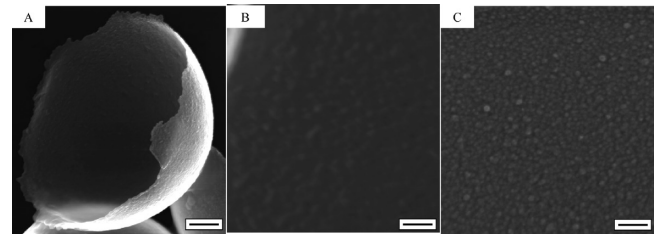

FIGURE 8. HR-SEM images of TiO_2 caps and thin films. (A) Image of a solvent-treated cap. Scale bar = 300 nm. (B) Higher magnification image of the internal surface of the cap at a 2 mm working distance (see the text). Scale bar = 50 nm. (C) Surface morphology of a TiO_2 thin film on a silicon wafer. Scale bar = 50 nm.

The similarity between the TiO_2 caps and thin films is further validated by HR-SEM imaging. The HR-SEM images of a cap and its inside surface and a TiO_2 thin film on a silicon wafer are shown in Figure 8. Figure 8A confirms clean removal of PS residues from the internal surface of the cap, as suggested by the absence of a carbon signal in the EDS data of the solvent-treated caps. Figure 8B shows a high-resolution image of the inside surface of the cap shown in Figure 8A. The surface is found to be grainy, with grains ranging from ~5 to ~15 nm. Note that the image appears to be out of focus because of the curved nature of the cap and the very short working distance (2 mm) used during the imaging. The former may result in a larger apparent size of the grains owing to the limited depth of the field. A comparison of Figure 8B with the thin film surface (Figure 8C) reveals a comparable surface morphology with somewhat smaller grains ($d = 7 \pm 4$ nm). HR-XPS spectra (Figure S1 in the Supporting Information) collected on the thin films confirm TiO_2 as the composition of the thin films (Table 2) (21, 33).

In an effort to determine the crystallinity and phase of the TiO_2 thin films, X-ray diffractometry (XRD), electron backscatter diffractometry (EBSD), and transmission electron microscopy (TEM) are performed on the thin films. No XRD and EBSD patterns are detected (Figures S2 and S3 in the Supporting Information) that would allow identification of the TiO_2 structure and phase. A possible rationale for this finding is that the 30 ± 3 nm TiO_2 films used are too thin. Usually thin films with thicknesses greater than 500 nm are used in XRD measurements, and grain domains greater than 50 nm are required for EBSD measurements (37−39).

While generally possible with our evaporation setup, the deposition of thicker TiO_2 films is complicated by the small size of the tungsten basket used in our PVD system. The small basket size requires reloading of the titanium sponge during evaporation, which may cause contamination of the films by exposure to air. In addition, the thicknesses of the films used for diffraction measurements should match the thicknesses of the caps used for the CMRs (~30 nm) to ensure comparability. Last but not least, TEM characterization was performed on TiO_2 thin films (30 nm) evaporated on TEM grids (Figure S4 in the Supporting Information). A comparison of the diffraction pattern of the TiO_2 thin film with that of a plain titanium film of comparable thickness suggests that the TiO_2 thin film is amorphous. Interestingly, Eufinger and co-workers (37) term thin TiO_2 films that are undetectable with XRD but show a short-range ordering (<10 nm) in HR-SEM "XRD amorphous". The TiO_2 cap and films used in this study (Figure 8) show TiO_2 grains ranging from 5 to 15 nm comparable to Eufinger's films. Therefore, we refer to our TiO_2 cap material as "XRD amorphous" TiO_2.

Eufinger and co-workers (37) further show that short-range ordering or small grains in "XRD amorphous" TiO_2 show an enhanced charge separation compared to larger grains (>40 nm), which leads to an increased photocatalytic activity (37, 40). The catalytic efficiency of "XRD amorphous" TiO_2 is cross-referenced with a commercially available Pilkington Active reference TiO_2 catalyst by Eufinger et al. (37) It is manufactured on a glass substrate with a 15 nm thin coating of anatase TiO_2 (41). The photocatalytic reaction rate of Pilkington Active is measured to be 0.34 ppm/min for ethanol breakdown. In comparison, the "XRD amorphous" TiO_2 reaction rate is measured to be 0.13 ppm/min for the same thickness (37). The photocatalytic reaction rate for ethanol breakdown increases to 1.3 ppm/min as the deposition thickness increases to 300 nm, indicating that "XRD amorphous" TiO_2 is an effective functional catalyst (37).

CONCLUSION

When CDTS is employed, increased precision and control of the physical characteristics and properties of multisectional, TiO_2-loaded CMRs are achieved. We have shown that properties such as the reactor shape and size, pore structure, pore-size distribution, and catalyst distribution within the CMR are the parameters that are controlled using CDTS. Careful analysis of the catalyst material with EDS and XPS ensures the cleanliness and correct composition of the TiO_2 catalyst. While the thinness of the catalyst caps prevents the structural characterization of TiO_2 with XRD techniques, HR-SEM and TEM identify the catalyst as "XRD amorphous" TiO_2. The described methodology can be extended to other catalysts that can be deposited by PVD (45), geometries accessible to colloidal assembly (46), and types of polymers that can be infiltrated and cured (47).

Acknowledgment. The authors thank Hernan Rengifo at Columbia University's Department of Chemical Engineering for assistance with the XPS measurements and Jorge Morales of CCNY's EM Center for his assistance with HR-SEM and TEM. Glen Kowach and Chun-min Feng are acknowledged for assisting the authors with XRD measurements and for insightful discussion. This work was support by the National Science Foundation under Award CBET 0625753.

Supporting Information Available: XPS, XRD, EBSD, and TEM. This material is available free of charge via the Internet at http://pubs.acs.org.

REFERENCES AND NOTES

(1) Dittmeyer, R.; Hollein, V.; Daub, K. *J. Mol. Catal. A: Chem.* **2001**, *173*, 135.
(2) Stankiewicz, A. *Chem. Eng. Process.* **2003**, *42*, 137.
(3) Vankelecom, I. F. J. *Chem. Rev.* **2002**, *102*, 3779.
(4) Vankelecom, I. F. J.; Vercruysse, K. A. L.; Neys, P. E.; Tas, D. W. A.; Janssen, K. B. M.; Knops-Gerrits, P. P.; Jacobs, P. A. *Top. Catal.* **1998**, *5*, 125.
(5) Stankiewicz, A. *Chem. Eng. Res. Des.* **2006**, *84*, 511.
(6) Ozdemir, S. S.; Buonomenna, M. G.; Drioli, E. *Appl. Catal., A* **2006**, *307*, 167.
(7) Dixon, A. G. *Int. J. Chem. Reactor Eng.* **2003**, *1*, 1.
(8) Song, J. H.; Kretzschmar, I. *Langmuir* **2008**, *24*, 10616.
(9) Perro, A.; Reculusa, S.; Ravaine, S.; Bourgeat-Lami, E. B.; Duguet, E. *J. Mater. Chem.* **2005**, *15*, 3745.
(10) Smoukov, S. K.; Gangwal, S.; Marquez, M.; Velev, O. D. *Soft Matter* **2009**, *5*, 1285.
(11) Chen, X.; Mao, S. S. *Chem. Rev.* **2007**, *107*, 2891.
(12) Feng, B.; Chen, J. Y.; Qi, S. K.; He, L.; Zhao, J. Z.; Zhang, X. D. *J. Mater. Sci.: Mater. Med.* **2002**, *13*, 457.
(13) Kasemo, B. *J. Prost. Dent.* **1983**, *49*, 832.
(14) Quinn, R. K.; Armstrong, N. R. *J. Electrochem. Soc.* **1978**, *125*, 1790.
(15) Armstrong, N. R.; Quinn, R. K. *Surf. Sci.* **1977**, *67*, 451.
(16) Li, Y. L.; Ishigaki, T. *Chem. Mater.* **2001**, *13*, 1577.
(17) Chen, G. S.; Lee, C. C.; Niu, H.; Huang, W.; Jann, R.; Schutte, T. *Thin Solid Films* **2008**, *516*, 8473.
(18) Giolli, C.; Borgioli, F.; Credi, A.; Di Fabio, A.; Fossati, A.; Miranda, M. M.; Parmeggiani, S.; Rizzi, G.; Scrivani, A.; Troglio, S.; Tolstoguzov, A.; Zoppi, A.; Bardi, U. *Surf. Coat. Technol.* **2007**, *202*, 13.
(19) Kwon, S.; Fan, M.; Cooper, A. T.; Yang, H. Q. *Crit. Rev. Environ. Sci. Technol.* **2008**, *38*, 197.
(20) Carp, O.; Huisman, C. L.; Reller, A. *Prog. Solid State Chem.* **2004**, *32*, 33.
(21) Yu, J. C.; Yu, J. G.; Ho, W. K.; Jiang, Z. T.; Zhang, L. Z. *Chem. Mater.* **2002**, *14*, 3808.
(22) Sibu, C. P.; Kumar, S. R.; Mukundan, P.; Warrier, K. G. K. *Chem. Mater.* **2002**, *14*, 2876.
(23) Hong, X. T.; Wang, Z. P.; Cai, W. M.; Lu, F.; Zhang, J.; Yang, Y. Z.; Ma, N.; Liu, Y. J. *Chem. Mater.* **2005**, *17*, 1548.
(24) Zhang, Y. H.; Ebbinghaus, S. G.; Weidenkaff, A.; Kurz, T.; von Nidda, H. A. K.; Klar, P. J.; Gungerich, M.; Reller, A. *Chem. Mater.* **2003**, *15*, 4028.
(25) Prevo, B. G.; Velev, O. D. *Langmuir* **2004**, *20*, 2099.
(26) NIST. *NIST X-ray Photoelectron Spectroscopy Database*; National Institute of Standards and Technology: Washington, DC, 2003.
(27) Li, S. P.; Qin, Y. J.; Shi, J. H.; Guo, Z. X.; Yongfang, L.; Zhu, D. B. *Chem. Mater.* **2005**, *17*, 130.
(28) Pawar, A. B.; Kretzschmar, I. *Langmuir* **2008**, *24*, 355.
(29) Kalyanasundaram, K.; Gratzel, M. *Coord. Chem. Rev.* **1998**, *177*, 347.
(30) Love, J. C.; Gates, B. D.; Wolfe, D. B.; Paul, K. E.; Whitesides, G. M. *Nano Lett.* **2002**, *2*, 891.
(31) Gates, B.; Yin, Y. D.; Xia, Y. N. *Chem. Mater.* **1999**, *11*, 2827.
(32) Velev, O. D.; Jede, T. A.; Lobo, R. F.; Lenhoff, A. M. *Chem. Mater.* **1998**, *10*, 3597.
(33) Miller, S.; Berning, G. L. P.; Plank, H.; Roth, J. *J. Vac. Sci. Technol., A* **1997**, *15*, 2029.
(34) Arvieu, C.; Manaud, J. P.; Quenisset, J. M. *J. Alloys Compd.* **2004**, *368*, 116.
(35) Cui, J. Q.; Kretzschmar, I. *Langmuir* **2006**, *22*, 8281.

(36) Cahill, D. G.; Allen, T. H. *Appl. Phys. Lett.* **1994**, *65*, 309.
(37) Eufinger, K.; Poelman, D.; Poelman, H.; De Gryse, R.; Marin, G. B. *Appl. Surf. Sci.* **2007**, *254*, 148.
(38) Dingley, D. J.; Randle, V. *J. Mater. Sci.* **1992**, *27*, 4545.
(39) Wilkinson, A. J.; Hirsch, P. B. *Micron* **1997**, *28*, 279.
(40) Nam, H. J.; Amemiya, T.; Murabayashi, M.; Toh, K. *J. Phys. Chem. B* **2004**, *108*, 8254.
(41) Mills, A.; Lepre, A.; Elliott, N.; Bhopal, S.; Parkin, I. P.; O'Neill, S. A. *J. Photochem. Photobiol., A* **2003**, *160*, 213.
(42) Galuska, A. A.; Uht, J. C.; Marquez, N. *J. Vac. Sci. Technol., A* **1988**, *6*, 110.
(43) Gonbeau, D.; Guimon, C.; Pfisterguillouzo, G.; Levasseur, A.; Meunier, G.; Dormoy, R. *Surf. Sci.* **1991**, *254*, 81.
(44) Werfel, F.; Brummer, O. *Phys. Scr.* **1983**, *28*, 92.
(45) Mattox, D. M. *Handbook of Physical Vapor Deposition (PVD) Processing: Film Formation, Adhesion, Surface Preparation and Contamination Control*; Noyes Publications: Westwood, NJ, 1998.
(46) Zhang, J.; Sun, Z.; Yang, B. *Curr. Opin. Colloid Interface Sci.* **2009**, *14*, 103.
(47) Li, Q.; Retsch, M.; Wang, J.; Knoll, W.; Jonas, U. *Templates in Chemistry III*; Topics in Current Chemistry; Springer-Verlag: Berlin, 2009; Vol. 287, p 135.

AM900286K